

Biostratigraphic refinement of tetrapod-bearing beds from the Metangula Graben (Niassa Province, Mozambique). New radiometric dating and the first Lower Triassic tetrapod fossils from Mozambique

Ricardo Araújo^{1*}  [§], Zanildo Macungo^{2,3} , Roger M.H. Smith^{3,4} , Stephen Tolan⁵,

Kenneth D. Angielczyk⁶, James Crowley⁷, Dino Milisic², João Mugabe⁸

¹Instituto de Plasmas e Fusão Nuclear, Instituto Superior Técnico, Universidade de Lisboa, Av. Rovisco Pais 1, Lisboa, Portugal

²Museu Nacional de Geologia, Av. 24 de Julho nº355, Maputo, Mozambique

³Evolutionary Studies Institute (ESI), School of Geosciences, University of the Witwatersrand, Johannesburg, 2050 South Africa

⁴Karoo Palaeontology, Iziko South African Museum, Cape Town 8000, South Africa

⁵Chipembele Wildlife Education Centre, Chowa Site, Malama Road, Mfuwe, Zambia

⁶Negaunee Integrative Research Center, Field Museum of Natural History, 1400 South Lake Shore Drive, Chicago, IL, 60605, U.S.A.

⁷Boise State University, Department of Geosciences, Boise, ID, 83725-1535, U.S.A.

⁸Departamento de Geologia, Universidade Eduardo Mondlane, Maputo, Mozambique

Received 6 March 2020. Accepted 10 November 2020

Numerous fossils of the toothed dicynodont *Endothiodon* have been collected previously from the Permian K5 formation of the Metangula Graben (Niassa, Mozambique). However, no identifiable vertebrate fossils have been reported from other stratigraphic units in the basin. Here we report likely Triassic tetrapod remains from the base of the Fubué Formation some 700 stratigraphic metres above the dated K5 Formation. We present anatomical comparisons and a phylogenetic analysis that confirm that they have close affinities to the well-known Early Triassic dicynodont therapsid *Lystrosaurus*. Thus, the Metangula Graben can now join the few regions in the world that preserve terrestrial tetrapod fossils from before and after Permian-Triassic mass extinction event, giving it the potential to provide further insights into the evolution of terrestrial organisms during this major biotic crisis. We present an updated geological section and paleoenvironmental interpretations, as well as the first assessment of the vertebrate taphonomy of the K5, K6, Mount Lilonga, and Fubué Formations. We also report the first radiometric dates for the K5c member of the K5 formation. The K5c has a maximum depositional age of 258.85 ± 0.41 Ma and is thus older than previously thought, falling near the boundary between the *Lycosuchus-Eunotosaurus* and *Tropidostoma-Gorgonops* subzones of the *Endothiodon* Assemblage Zone, rather than being coeval with the *Cistecephalus* Assemblage Zone.

Keywords: *Lystrosaurus*, Dicynodontia, Fubué Formation, radiometric dating, Permian-Triassic Mass Extinction.

Palaeontologia africana 2020. ©2020 Ricardo Araújo, Zanildo Macungo, Roger M.H. Smith, Stephen Tolan, Kenneth D. Angielczyk, James Crowley, Dino Milisic, João Mugabe. This is an open-access article published under the Creative Commons Attribution 4.0 Unported License (CC BY4.0). To view a copy of the license, please visit <http://creativecommons.org/licenses/by/4.0/>. This license permits unrestricted use, distribution, and reproduction in any medium, provided the original author and source are credited.

The article is permanently archived at: <https://hdl.handle.net/10539/30352>

INTRODUCTION

Few Gondwanan basins preserve a detailed palaeontological record of the effects of the Permian-Triassic mass extinction on tetrapods. By far the most studied record is that of the South African main Karoo Basin, but the placement of the Permian-Triassic boundary in this sequence and the severity of the extinction recorded there have been the subject of recent debate (e.g. Smith & Botha-Brink 2014; Gastaldo *et al.* 2015, 2017, 2018; 2019a,b, 2020; Lucas 2017; Viglietti *et al.* 2018; Botha *et al.* 2020). Continental basins in Antarctica, Argentina, Australia, Brazil, India, Kenya, Madagascar, Namibia, Tanzania, Uruguay, and Zambia have also produced Permian-Triassic tetrapod fossils, but all suffer from uncertainties regarding the

placement of the Permian-Triassic boundary and/or fossil records that provide information only about late Permian or Early Triassic tetrapods (e.g. Harris & Carroll 1977; Warren *et al.* 2001, 2006, 2011; Ketchum & Barrett 2004; Ray 2005; Abdala & Smith 2009; Modesto & Botha-Brink 2010; Sidor *et al.* 2010; Rozefelds *et al.* 2011; Angielczyk *et al.* 2014a,b; Ezcurra *et al.* 2015; Piñeiro *et al.* 2015; Valdiya 2016; Eltink *et al.* 2017; Francischini *et al.* 2018; Smith *et al.* 2018; Peecook *et al.* 2019; Desojo *et al.* 2020). The Metangula Graben of northern Mozambique preserves an excellent sedimentary sequence spanning the Permian to the Early Jurassic (Verniers *et al.* 1989) but its fossil record has received comparatively little attention (Verniers *et al.* 1989; Latimer *et al.* 1995; Araújo *et al.* 2012, 2018a; Castanhinha *et al.* 2013; Macungo *et al.* 2020).

*Author for correspondence. E-mail: ricardo.araujo@tecnico.ulisboa.pt

However, its nearly continuous sequence of Permian-Triassic strata has excellent potential to provide a new window into the turnover of tetrapod faunas coincident with the Permian-Triassic biotic crisis (Fig. 1).

A recent expedition to the Metangula Graben in October 2019, under the auspices of the PaleoMoz Project (www.paleomoz.org), greatly expanded the number of vertebrate fossil localities from the informally named K5 and K6 units, through the Mount Lilonga Formation and into the lowermost Fubué Formation (Ksb, of Verniers *et al.* 1989), and is part of a more general re-assessment of the palaeontological heritage of Mozambique (Araújo *et al.* 2018a,b; Flores *et al.* 2019; Macungo *et al.* 2020). The top of the K5 formation is early Lopingian, but most of it is probably Guadalupian (see below) and the Fubué Formation is Early Triassic, based on stratigraphic correlations and palynology-based biostratigraphy (Verniers *et al.* 1989). Here we report the first Triassic fossil vertebrate remains from Mozambique, which were collected from the Fubué Formation in the Lago District of Niassa Province. Among the material is a dicynodont maxilla that closely resembles *Lystrosaurus*, the quintessential Early

Triassic tetrapod disaster taxon, confirming the potential of the Metangula Graben as a source of information about the Permian-Triassic extinction. We also present new detrital zircon radiometric ages from the underlying K5 Formation. Together, these results facilitate more reliable biostratigraphic comparisons of the Metangula Graben sedimentary sequence with those of other Gondwanan terrestrial sedimentary basins.

Geological description and palaeoenvironmental interpretation

The K5 Formation can be divided into three successive members: K5a, K5b and K5c. The lithology of the K5a member consists of dark grey and reddish-grey massive siltstones with minor tabular fine-grained sandstone interbeds. Sandstones with calcite cement weather out as low ridges. Horizons of spheroidal calcareous nodules (3–20 cm in diameter) with internal septarian shrinkage structures occur within the thick mudrock sequences. The palaeoenvironmental interpretation of K5a is one of well-drained and fully-vegetated river floodplains with generally high water tables that sustained standing water

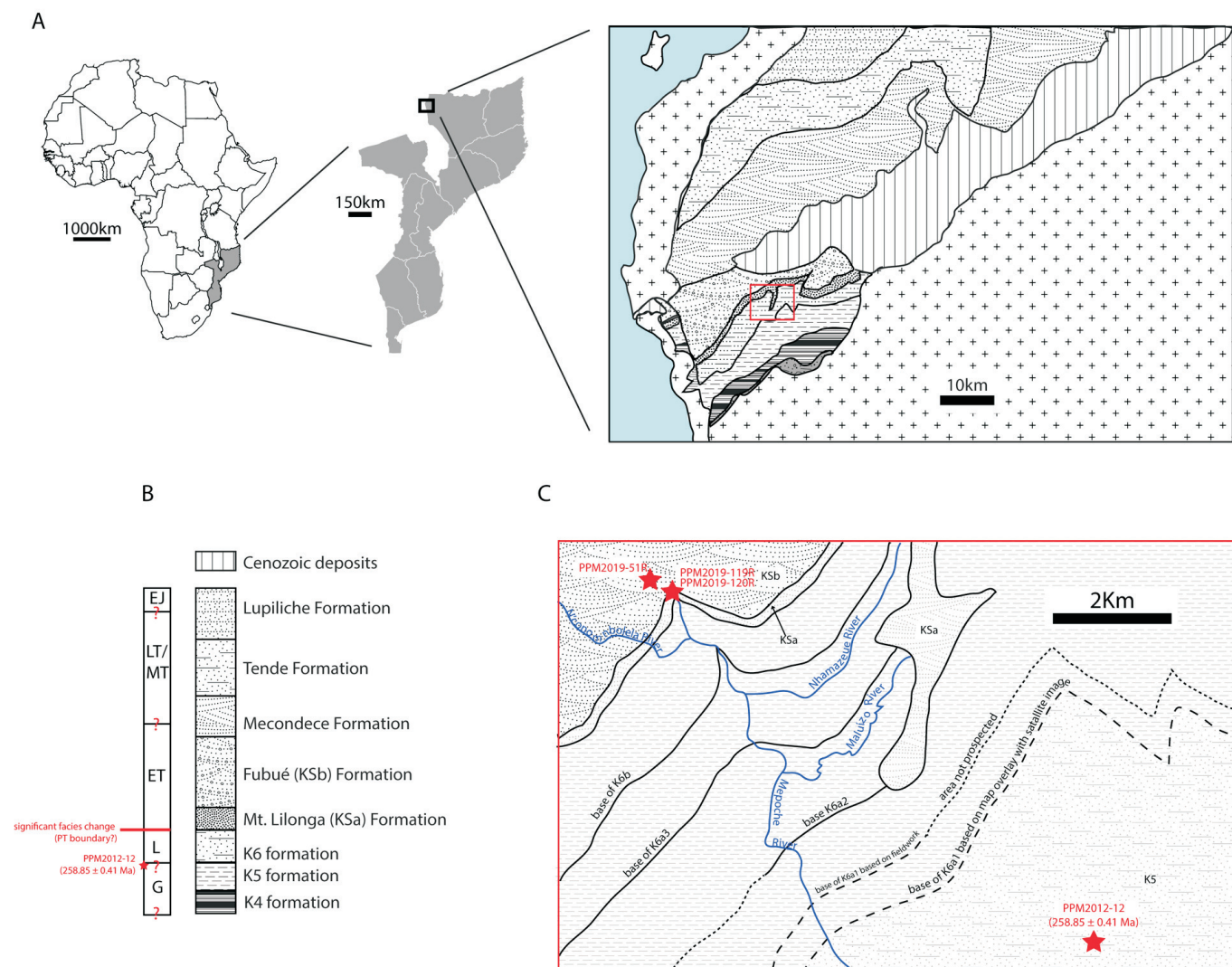


Figure 1. Geography and geology of the study site. **A**, Location of Mozambique in Africa, the location of the Metangula Graben in Mozambique, and the location and geology of the Metangula Graben. **B**, Chronostratigraphic column based on Verniers *et al.* 1989. **C**, Formations and respective members of the studied sites. Location of the sample taken for radiometric dating and the location and stratigraphic position of PPM2019-51R (red stars). G, Guadalupian; L, Lopingian; ET, Early Triassic; MT, Middle Triassic; LT, Late Triassic; EJ, Early Jurassic.

bodies in lowland depressions (Kreuser 1995). To date, only fossil tree trunks have been recovered from this member, as found by our team in the 2019 PaleoMoz Expedition.

The K5b member is approximately 60 metres thick and comprises generally coarser sandy-siltstone with sandier intervals that display ripple cross-lamination and clay-stone-veneered oscillation-rippled palaeosurfaces. Dark grey lenses of carbonaceous detrital leaf trash occur in places. Near the base of the member are several horizons of calcareous nodules, some of which contain therapsid bones. The interpreted depositional environment for K5b is a wetland alluvial plain with ponds, lakes and vegetated islands (e.g. Yemane & Kelts 1990). The taphonomic signature of this interval is one of disarticulated and scattered *Endothiodon* skeletons, most but not all of which are encrusted with calcareous nodular material. Many of these bones have been 'exploded' by disruptive micrite precipitation in cavities.

The K5c member comprises reddish grey very fine-grained sandstone, siltstone and indurated claystone. Near the base, there are several horizons of large (up to 70 cm long) elongated calcareous nodules that have a distinctive vertical orientation in the field, perpendicular to the strata. At the top of the member, there are several thin horizons of horizontally-oriented oblate iron-rich nodules, some of which contain therapsid bones. The palaeoenvironmental interpretation of K5c is of a vegetated river floodplain with groundwater-fed ponds that seasonally fluctuated in water depth and salinity (Verniers *et al.* 1989; Kreuser 1995). Confirmed fossils from this unit include *Endothiodon* skull and skeletal elements, small and medium-sized dicynodonts such as *Niassodon mfumukasi*, a partial gorgonopsian skull, non-marine bivalves (e.g. Antunes 1975; Castanhinha *et al.* 2013; Macungo *et al.* 2020; Verniers *et al.* 1989), and tree trunk fragments found by our 2019 PaleoMoz Expedition. The taphonomic style is characterized by accumulations of scattered but associated *Endothiodon* skeletons along with isolated bones likely concentrated around margins of ponds. The *Endothiodon* bones have a pervasive reddish-grey bone colour, and most are partially or wholly encrusted with micritic calcareous nodular material. The small and medium-sized dicynodonts from higher in the succession are preserved as both articulated and scattered but still associated skeletons in hematite-rich rough-surfaced nodules. The radiometric dating sample PPN2012-12 was collected from this member (Fig. 1).

The K6 Formation comprises four members K6a1, K6a2, K6a3 and K6b. The base of the K6a1 member is marked by a 3–5 m-thick fine to medium-grained, vertically-accreted, trough cross-bedded sandstone. The upper contact of this sandstone with the overlying mudrocks is characteristically sharp and gently undulating with distinctive current rippled surfaces. The overlying mudrocks comprise grey and greenish-grey massive siltstones with minor interbedded sheets of indurated green claystone and calcareous siltstone (calcilitute). The latter displays fine horizontal and ripple-cross lamination. The palaeoenvironment is interpreted as a riverine braidplain giving way to flood-

plain and lacustrine-dominated environments (Yemane & Kelts 1990). There are impressions of *Glossopteris* leaves toward the top of the member. Smooth-surfaced micrite nodules containing fragmented skeletal and cranial elements of therapsids with a distinctive black colour occur in the mudrock interval.

The K6a2 member begins with a 3–5 m-thick vertically accreted yellowish-brown fine to coarse-grained pebbly arkosic wacke structured with trough cross-bedding, giving way to planar cross-bedding. A smooth hummocky top surface in coarse sandstone is in sharp contact with the overlying olive and dark grey mudrock succession. The palaeoenvironment is interpreted as an axial braided channel giving way to predominantly wet overbank environments similar to that described by Smith (2000) from equivalent-aged rift basin sediments in Madagascar. The fossil content of the K6a2 member consists of few *Glossopteris* impressions in carbonaceous 'seamlets' as well as several complete *Dapocephalus*-like medium to large dicynodont skulls and their isolated postcranial elements (PPM2019-32Z fossil site) with distinctive black bone colour. The K6a3 member begins with a laterally continuous multistoried vertically-accreted fine-grained sandstone mainly structured with wave ripples. This 5 m-thick sandstone is topped by a calcified trough cross-bedded very fine-grained sandstone unit with a west-south-westerly palaeocurrent direction that sharply contacts a thick unit of mottled olive and brown massive mudstone and siltstone with horizons of gypsum rosettes. The palaeoenvironmental interpretation of this member is a more distal braidplain with drier and better-drained floodplains than lower in the succession. Similar replaced gypsum desert-rose structures have been described from the Balfour Formation of the main Karoo Basin, which are interpreted as an indication of temporary alkaline lakes on the floodplains (Smith 1990). Fossils comprise silicified wood fragments and a few black bone fragments.

The K6b member begins with a laterally continuous 4 m-thick fine-grained sandstone structured at base with horizontal lamination, passing upwards into trough cross-bedding capped by ripple cross-stratification. The overlying 50 m-thick succession of floodplain fines is dominated by alternating siltstone and fine-grained sandstone beds and massive green/brown mottled mudstone. The mudstones display root structures and incipient pedogenesis. The interpreted depositional setting is a broad, shallow, low-sinuosity channel belt giving way to seasonally dry floodplain environments (*cf.* Smith 1990). The fossils recovered from this unit are isolated fragments of black bone and pieces of silicified wood. The detrital zircon sample PPM2019-120R was collected from the top of this unit.

The ~300 metres of strata immediately underlying the fossiliferous base of the Fubué Formation is the Mount Lilonga Formation (Fig. 1). This formation conformably overlies the K6b member with a laterally-continuous, cliff-forming, coarse-grained trough cross-bedded conglomeratic arkosic wackestone. Extrabasinal pebble-sized rounded and subrounded clasts of quartzite and metamorphics are present along with intraformationally-derived

mudrock clods. Only fragments of fossil tree trunks have been retrieved from this formation. We interpret the depositional setting of the Mt Lilonga Fm. as a mid-fan braided river system. The upper facies of the Mt Lilonga Fm. are poorly exposed, but from the few river cuts it comprises green and greenish-grey sandy-siltstone with medium-grained sandstone lenses. The detrital zircon sample PPM2019-119R was collected from the bottom of this unit.

The Fubué Formation (KSb, Fig. 1) sharply and conformably overlies the Mt Lilonga Fm. and is composed of at least 100 m of vertically-stacked units of trough cross-bedded white-weathering quartz gritstone. The bedding planes are marked by purple staining that highlights zones of convolute and overturned bedding. The erosive bases of these 4–10-metre-thick units are lined with a single layer of well-rounded extrabasinal quartz and quartzite pebbles. The fossil remains described here were found close to the base of the Fubué Formation and comprise isolated dicynodont cranial and postcranial fragments, as well as fossil tree trunk fragments. The fossils display evidence of preburial fragmentation and abrasion that likely occurred during transportation of the disarticulated elements in high-velocity currents. We interpret the depositional setting as an expansive vertically-aggrading braidplain in the mid to upper regions of a large distributary fan (*cf.* Weissman *et al.* 2010). Verniers *et al.* (1989) suggested a similar palaeoenvironment, but they did not recover fossils from this formation during their geological reconnaissance.

MATERIALS AND METHODS

Material

The material collected at the base of the Fubué Formation comprises a right maxilla (PPM2019-51R/A, Figs 2 & 3), a partial left maxilla (PPM2019-51R/B, Fig. 2), a right dorsal rib (PPM2019-51R/D, Fig. 4), a partial left tusk (PPM2019-51R/E, Fig. 4), a distal right fibula (PPM2019-51R/F, Fig. 4), a vertebral centrum (PPM2019-51R/G), and a distal left femur (PPM2019-51R/C, Fig. 5).

LA-ICPMS methods

Rock samples for dating a specific stratigraphic level were collected by opening a small quarry to remove surficial rock and collecting a fresh sample that was labelled and stored in a closed plastic bag. The subsequent analyses were done at the Boise State University Geochronology Lab. Zircon grains were separated using standard techniques, annealed at 900°C for 60 h in a muffle furnace, and mounted in epoxy and polished until their centres were exposed. The analyses were done at the Boise State University Isotope Geology Lab. Cathodoluminescence (CL) images were obtained with a JEOL JSM-1300 scanning electron microscope and Gatan MiniCL. Zircon was analysed by laser ablation inductively coupled plasma mass spectrometry (LA-ICPMS) using a ThermoElectron X-Series II quadrupole ICPMS and New Wave Research UP-213 Nd:YAG UV (213 nm) laser ablation system. In-house analytical protocols, standard

materials, and data reduction software were used for acquisition and calibration of U-Pb dates as well as a suite of high field strength elements (HFSE) and rare earth elements (REE). Zircon was ablated with a laser spot of 25 µm width using fluence and pulse rates of 5 J/cm² and 10 Hz, respectively, during a 45 second analysis (15 sec gas blank, 30 sec ablation) that excavated a pit ~25 µm deep. Ablated material was carried by a 1.2 l/min He gas stream to the nebulizer flow of the plasma. Dwell times were 5 ms for Si and Zr, 200 ms for ⁴⁹Ti and ²⁰⁷Pb, 80 ms for ²⁰⁶Pb, 40 ms for ²⁰²Hg, ²⁰⁴Pb, ²⁰⁸Pb, ²³²Th, and ²³⁸U and 10 ms for all other HFSE and REE. Background count rates for each analyte were obtained prior to each spot analysis and subtracted from the raw count rates for the analytes. Ablation pits that appear to have intersected glass or mineral inclusions were identified based on Ti and P. U-Pb dates from these analyses are considered valid if the U-Pb ratios appear to have been unaffected by the inclusions. Analyses that appear contaminated by common Pb were rejected based on mass 204 being above baseline. For concentration calculations, background-subtracted count rates for each analyte were internally normalized to ²⁹Si and calibrated with respect to NIST SRM-610 and -612 glasses as the primary standards. Temperature was calculated from the Ti-in-zircon thermometer (Watson *et al.* 2006). Because there are no constraints on the activity of TiO₂, an average value in crustal rocks of 0.8 was used.

Data from three samples were collected in separate experiments. For U-Pb and ²⁰⁷Pb/²⁰⁶Pb dates, instrumental fractionation of the background-subtracted ratios was corrected and dates were calibrated with respect to interspersed measurements of zircon standards and reference materials. The primary standard Plešovice zircon (Sláma *et al.* 2008) was used to monitor time-dependent instrumental fractionation based on two analyses for every 10 analyses of unknown zircon. A secondary correction to the ²⁰⁶Pb/²³⁸U dates was made based on results from the zircon standards Seiland (530 Ma, unpubl. data, Boise State University) and Zirconia (327 Ma, unpubl. data, Boise State University), FC1 (1098 Ma, unpubl. data, Boise State University), and AUSZ2 (Kennedy *et al.* 2014), which were treated as unknowns and measured once for every 10 analyses of unknown zircon. These results showed a linear age bias of several percent that is related to the ²⁰⁶Pb count rate. The secondary correction is thought to mitigate matrix-dependent variations due to contrasting compositions and ablation characteristics between the Plešovice zircon and other standards (and unknowns).

Radiogenic isotope ratio and age error propagation for all analyses includes uncertainty contributions from counting statistics and background subtraction. The standard calibration uncertainty for ²⁰⁶Pb/²³⁸U is 0.5–0.6% (2σ), which is the local standard deviation of the polynomial fit to the fractionation factor of Plešovice *versus* time. Age interpretations are based on ²⁰⁷Pb/²⁰⁶Pb dates for analyses with ²⁰⁷Pb/²⁰⁶Pb and ²⁰⁶Pb/²³⁸U dates >1000 Ma. Otherwise, interpretations are based on ²⁰⁶Pb/²³⁸U dates. Analyses with ²⁰⁶Pb/²³⁸U dates >1000 Ma and >20% positive discordance or >10% negative discordance are not considered. Errors on the dates are at 2σ.

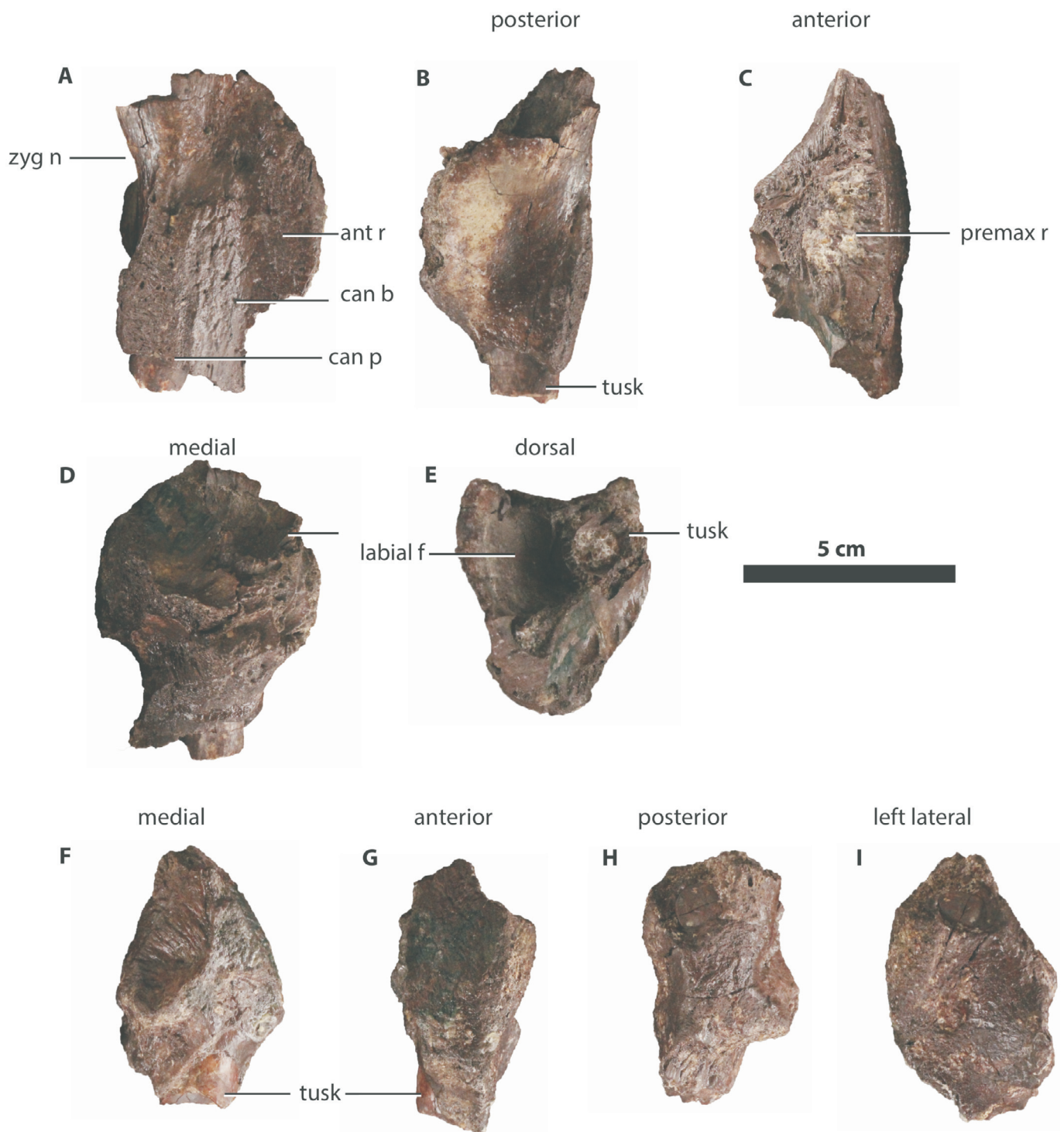


Figure 2. PPM2019-51R/A right maxilla and PPM2019-51R/B left maxilla from the Fubué Formation of the Metangula Graben (Mozambique). **A**, right lateral view; **B**, posterior view; **C**, anterior view; **D**, medial view. PPM2019-51R/A: **E**, dorsal view; **F**, left lateral view; **G**, posterior view; **H**, anterior view. PPM2019-51R/B: **I**, medial view.

CA-TIMS U-Pb geochronology methods

U-Pb dates were obtained by the chemical abrasion isotope dilution thermal ionization mass spectrometry (CA-TIMS) method from analyses composed of single zircon grains (Supplementary Data 1 and 2, see also the results for PPN2012-12 in Fig. 6), modified after Mattinson (2005), that were removed from mounts after LA-ICPMS. Zircon was put into 3 ml Teflon PFA beakers and loaded into 300 μ l Teflon PFA microcapsules. Fifteen microcapsules were placed in a large-capacity Parr vessel and the

zircon partially dissolved in 120 μ l of 29 M HF for 12 h at 190°C. Zircon was returned to 3 ml Teflon PFA beakers, HF was removed, and zircon was immersed in 3.5 M HNO₃, ultrasonically cleaned for an hour, and fluxed on a hot-plate at 80°C for an hour. The HNO₃ was removed and zircon was rinsed twice in ultrapure H₂O before being reloaded into the 300 μ l Teflon PFA microcapsules (rinsed and fluxed in 6 M HCl during sonication and washing of the zircon) and spiked with the EARTHTIME 2535 mixed ²³³U-²³⁵U-²⁰²Pb-²⁰⁵Pb tracer solution. Zircon was dissolved

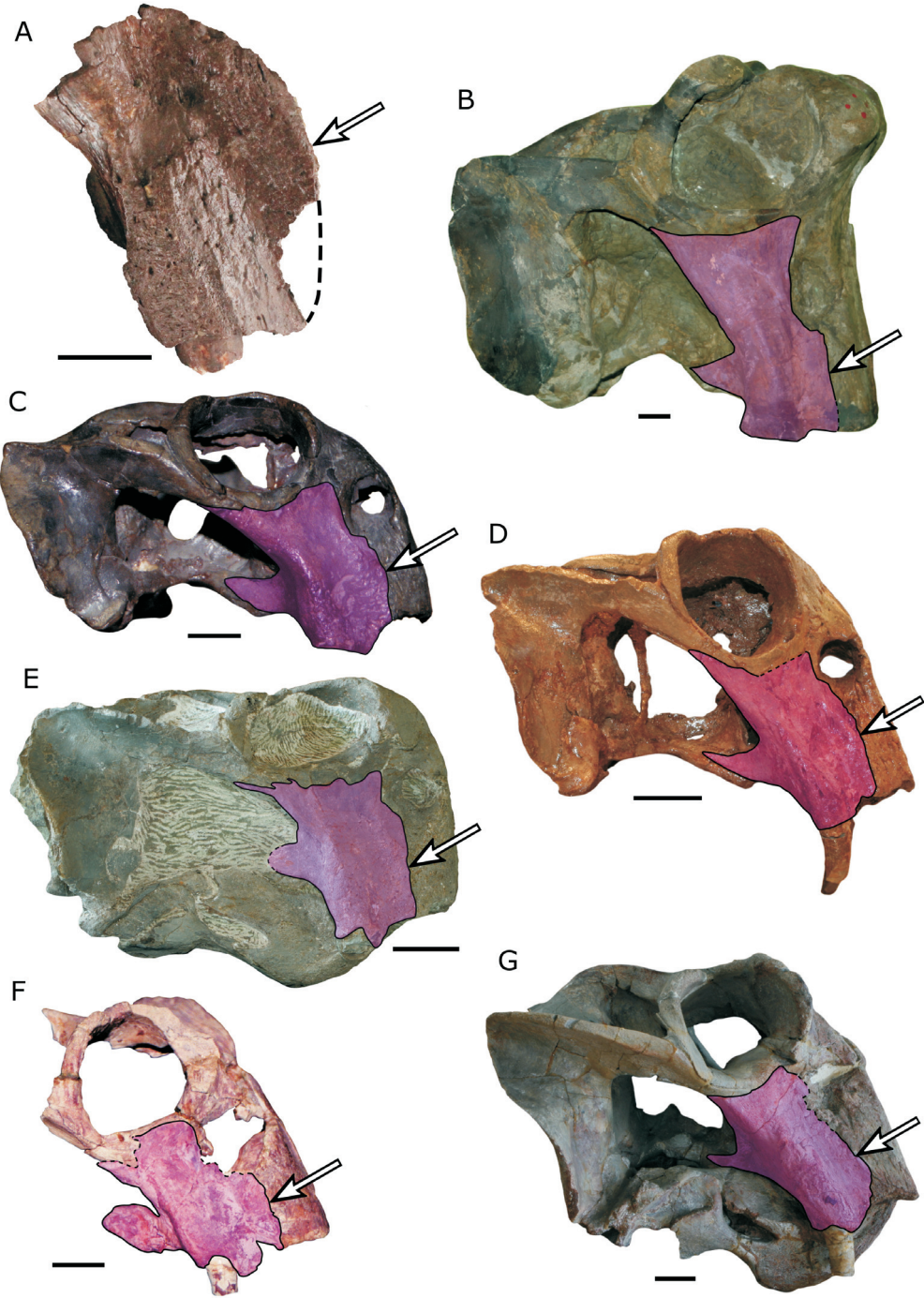


Figure 3. Lateral view of the maxillary in the various *Lystrosaurus* species. **A**, PPM2019-51R/A; **B**, *L. maccaigi* (BP/1/879); **C**, *L. curvatus* (NMQR 3595); **D**, *L. declivis* (NMQR 815); **E**, *L. murrayi* (SAM-PK-K10466); **F**, *L. georgi* (PIN 3447/1); **G**, *L. hedini* (IVPP V 3243).

in Parr vessels in 120 μl of 29 M HF with a trace of 3.5 M HNO₃ at 220°C for 48 h, dried to fluorides, and re-dissolved in 6 M HCl at 180°C overnight. U and Pb were separated from the zircon matrix using an HCl-based anion-exchange chromatographic procedure (Krogh 1973), eluted together and dried with 2 μl of 0.05 N H₃PO₄.

Pb and U were loaded on a single outgassed Re filament in 5 μl of a silica-gel/phosphoric acid mixture (Gerstenberger & Haase 1997), and U and Pb isotopic measurements made on a GV Isoprobe-T multicollector thermal ionization mass spectrometer equipped with an ion-counting Daly detector. Pb isotopes were measured by peak-jumping all isotopes on the Daly detector for 160 cycles, and corrected for $0.16 \pm 0.06\%$ /a.m.u. (2σ) mass

fractionation. Transitory isobaric interferences due to high-molecular weight organics, particularly on ²⁰⁴Pb and ²⁰⁷Pb, disappeared within approximately 30 cycles, while ionization efficiency averaged 10⁴ cps/pg of each Pb isotope. Linearity (to $\geq 1.4 \times 10^6$ cps) and the associated deadtime correction of the Daly detector were determined by analysis of NBS982. Uranium was analysed as UO₂⁺ ions in static Faraday mode on 10¹² ohm resistors for 300 cycles, and corrected for isobaric interference of ²³³U¹⁸O¹⁶O on ²³⁵U¹⁶O¹⁶O with an ¹⁸O/¹⁶O of 0.00206. Ionization efficiency averaged 20 mV/ng of each U isotope. U mass fractionation was corrected using the known ²³³U/²³⁵U ratio of the EARTHTIME tracer solution.

CA-TIMS U-Pb dates and uncertainties were calcu-

lated using the algorithms of Schmitz & Schoene (2007), EARTHTIME ET2535 tracer solution (Condon *et al.* 2015) with calibration of $^{235}\text{U}/^{205}\text{Pb} = 100.233$, $^{233}\text{U}/^{235}\text{U} = 0.99506$, $^{205}\text{Pb}/^{204}\text{Pb} = 8474$, and $^{202}\text{Pb}/^{205}\text{Pb} = 0.99924$ and U decay constants recommended by Jaffey *et al.* (1971) and $^{238}\text{U}/^{235}\text{U}$ of 137.818 from (Hiess *et al.* 2012). $^{206}\text{Pb}/^{238}\text{U}$ ratios and dates were corrected for initial ^{230}Th disequilibrium using $D_{\text{Th}/\text{U}} = 0.2 \pm 0.1$ (2σ) and the algorithms of Crowley *et al.* (2007), resulting in an increase in the $^{206}\text{Pb}/^{238}\text{U}$ dates of ~ 0.09 Ma. All common Pb in analyses was attributed to laboratory blank and subtracted based on the measured laboratory Pb isotopic composition and associated uncertainty. U blanks are estimated at 0.013 ± 0.018 pg (2σ). Errors are given at 2σ .

Phylogenetic analysis

To test the phylogenetic position of PPM2019-51R/A, we added it to the recent dicynodont-focused data matrix of Kammerer (2019). The modified matrix included 109 taxa, 173 discrete-state morphological characters, and 23 continuous morphometric characters. We analysed the data matrix using TNT 1.5 February 2020 version with no taxon limit for Windows (Goloboff & Catalano 2016). Morphological characters 58, 61, 79, 140, 150, 151, and 166 were ordered. The analysis used the 'FUSE' algorithm to find the most parsimonious trees, which took ~ 4 billion rearrangements and resulted in seven most parsimonious trees with a tree length of 1162.54. Once the best tree length was hit 20 independent times using 'xmult' plus 10 cycles of tree-drifting (Goloboff 1999), the strict consensus tree was drawn by collapsing the tree using tree bisection-reconnection and respective node supports. Synapomorphies common to all seven trees are shown in Fig. 7. Absolute and relative Bremer supports (Fig. 7) were calculated for the nodes by tree bisection-reconnection by swapping the trees (Bremer 1994; Goloboff & Farris 2001). We also used resampling to assess node support, which was calculated by doing 100 replications of symmetric resampling (Goloboff *et al.* 2003), analysing each dataset with a single random addition sequence plus tree bisection-reconnection and then collapsing the resulting tree (Goloboff & Farris 2001). For the complete trees with all branch supports and synapomorphies, as well as the two tree topologies where PPM2019-51R/A clusters with a monophyletic *Lystrosaurus* and with *Euptychognathus* see Supplementary Data 3. For the character matrix please see Supplementary Data 4.

RESULTS

Systematic palaeontology and comparative anatomical description

Synapsida Osborn, 1903

Therapsida Broom, 1905

Dicynodontia Owen, 1860

Lystrosauridae Broom, 1903

cf. Lystrosaurus sp.

In lateral view, the dominant feature of the maxilla PPM2019-51R/A is the caniniform buttress (can b), which

is more strongly developed ventrally, and becomes progressively flatter dorsally. The buttress steeply slopes anteriorly onto the subnarial portion of the maxilla (Fig. 2A–E). The ventralmost portion of the subnarial region is broken off, and none of the jugal and palatal processes are preserved. The caniniform process (can p), which extends ventrally beyond the subnarial region, is a short continuation of the caniniform buttress, and the maxillary tusk emerges from its ventral end. The tusk is oval in cross-section, with the long axis oriented labiolingually. The surface texture of the tusk is difficult to assess, as it is weathered and broken. The posterior edge of the maxilla is straight ventrally, and is marked by a smooth, concave recess (the zygomatic notch) that subtends the anteriormost inception of the zygomatic arch. The maxilla is heavily sculptured on the caniniform buttress by pits and corrugations, but the subnarial portion is much less ornamented and the surface that forms the zygomatic notch is smooth. In PPM2019-51R/A there is no anterior notch between the anterior edge of the caniniform process and the palatal rim as in ptylcephalids. The anterior edge of the maxilla, which contacts the premaxilla, is curved dorsally but becomes progressively straighter ventrally (Fig. 2A–E). The premaxillary facet on the medial surface of the maxilla is rugose and relatively flat. Damage to the dorsal surface of the maxilla has exposed the maxillary sinus (or maxillary antrum, max ant; e.g. Benoit *et al.* 2018), medial to the root of the tusk. PPM2019-51R/A can be ascribed to *cf. Lystrosaurus* sp. because of the relatively long, straight anterior border of the maxilla (Fig. 3), and the fact that the maxilla is significantly taller than wide, which is a byproduct of the ventrally elongated snout (Fig. 2). This attribution is partially corroborated by the results of our phylogenetic analysis (see below).

The maxilla PPM2019-51R/B (Fig. 2F–I) is heavily broken but possesses similar dimensions and proportions to PPM2019-51R/A. However, the surface texture of the tusk is better preserved in PPM2019-51R/B than in PPM2019-51R/A. The surface texture is completely smooth and does not show any indications of corrugations or infolding of the dentine such as described by Whitney *et al.* (2019).

Dicynodontia indet.. Owen, 1860

A partial left tusk (PPM2019-51R/E) was collected as float (Fig. 4A–C). The basal and apical portions of the tusk are not preserved and the lingual side is heavily broken. The lingual and labial sides can be identified based on the posterior curvature of tusk and its slight medial inflection. Therefore, both the labial and mesial sides are convex. The dimensions, curvature and smooth surface texture of PPM2019-51R/E closely resemble those of the tusks of PPM2019-51R/A and PPM2019-51R/B (Fig. 2), and there are apicobasal cracks that resemble the weathering pattern in PPM2019-51R/A. In cross-section, the tusk is slightly ellipsoidal with the long axis oriented labiolingually. The pulp-dentine ratio is $\sim 37\%$ of the long radius in cross-section.

Despite most of the periosteum on the articular surface being weathered off, a left fibula (PPM2019-51R/F) can

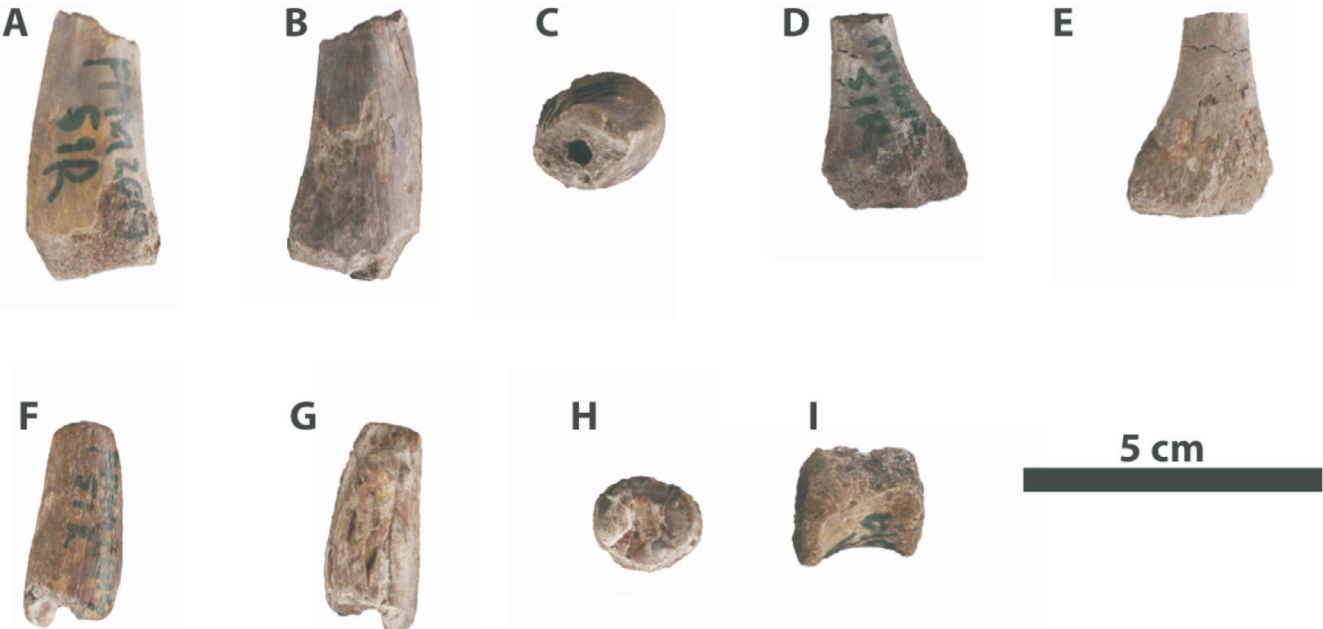


Figure 4. Dicynodontia indet. material from the Fubué Formation of the Metangula Graben (Mozambique). PPM2019-51R/E Dicynodontia indet. tusk: A, mesial view; B, distal view; C, root view. PPM2019-51R/F Dicynodontia indet. distal right fibula: D, anterior view; E, posterior view. F, PPM2019-51R/D Dicynodontia indet. dorsal right rib ventral view; G, dorsal view; H, distal view. PPM2019-51R/G Dicynodontia indet. small vertebra: I, lateral view.

be identified on the basis of the expanded 'golf club'-like shape of its distal end (Fig. 4D,E), which is typical of dicynodonts (e.g. Defauw 1986; King, 1981; Ray & Chinsamy 2003; Ray 2006). The medial side of the anterior surface is shallowly excavated, probably representing the iliofibularis insertion area (if). The distal articular surface is straight. The lateral edge curves laterally whereas the medial edge is more vertical.

A partial right dorsal rib (PPM2019-51R/D) was collected as float (Fig. 4F–H). The proximal head is missing as well as most of its distal portion. An incipiently developed costal groove is visible on the posteromedial side of the rib (Fig. 4A–C). The cortex of the rib is thin, and a thick cancellous region surrounds a well-developed central medullary cavity (Fig. 4A–C). The distal cross-section is diamond-shaped.

An isolated vertebral centrum (PPM2019-51R/G) was found near the rest of the material (Fig. 4I). The vertebra is amphicoelous, with thick articular facets giving a 'lipped' appearance in anterior and posterior views. It has a pronounced concave ventral edge, whereas the dorsal edge is straight and bears articular surfaces for the pedicles of the neural arch (Fig. 4I). The centrum is longer than wide or tall, which is common for dicynodont dorsal vertebrae (e.g. Angielczyk & Rubidge 2013; Kammerer 2018; Macungo *et al.* 2020).

A badly damaged distal left femur (PPM2019-51R/C) can still be identified on the basis of the preserved distal condyles (Fig. 5D–E). The periosteum on the distalmost portions of the preserved bone is missing. The angle between the distal articular surface and the medial border of the medial condyle (mc) forms a marked kink, whereas the lateral condyle (lc) is smoothly rounded as in most dicynodonts, including *Lystrosaurus* (Fig. 5A–C). A shallow intercondylar fossa separates the two distal condyles of the femur (Fig. 5D–E).

U-Pb geochronology results

The mineral separation from sample PPN2012-12 (K5c Member) contained tens of thousands of zircon grains, but only a small percentage (<0.1%) were sharply faceted and large enough to be mounted and polished for LA-ICPMS analysis. Twenty-seven sharply faceted grains were mounted, LA-ICPMS spots were placed on 18 grains, and 14 analyses were successful, yielding dates of 1292 ± 55 to 249 ± 4 Ma. The three youngest grains yielded CA-TIMS dates of 258.85 ± 0.41 , 259.81 ± 0.26 , and 264.46 ± 0.37 Ma. The youngest CA-TIMS date is interpreted as the maximum depositional age for the K5c member.

All zircon grains from sample PPM2019-119R (Mount Lilonga Formation) were large and sharply faceted. Forty-two grains yielded LA-ICPMS dates of 1069 ± 58 to 501 ± 24 Ma. Sample PPM2019-120R (K6b Member) has sharply faceted and round zircon. Twenty-three sharply faceted grains were large enough to be mounted and polished for LA-ICPMS analysis, and yielded LA-ICPMS dates of 1130 ± 47 to 495 ± 8 Ma. Because these samples were collected in strata that overlie the K5c member (i.e. the K6 and Mount Lilonga formations), we interpret these grains as recycled zircons that do not provide a useful constraint on the ages of these formations.

Phylogenetic results

The only element that we could code for phylogenetic analysis was the right maxilla PPM2019-51R/A. We coded characters 15, 20, 22, 23, 25, 27, 28, 29, 30 and 31 of Kammerer (2019) as follows: the maxilla of PPM2019-51R/A has a long caniniform process (char 15:1); the maxillary alveolar region is short (char 20:0); the maxillary canine is present as a tusk (char 22: 2); maxillary non-caniniform teeth are absent (char 23:2); there is a caniniform process (char 27:1); there is no caniniform depres-

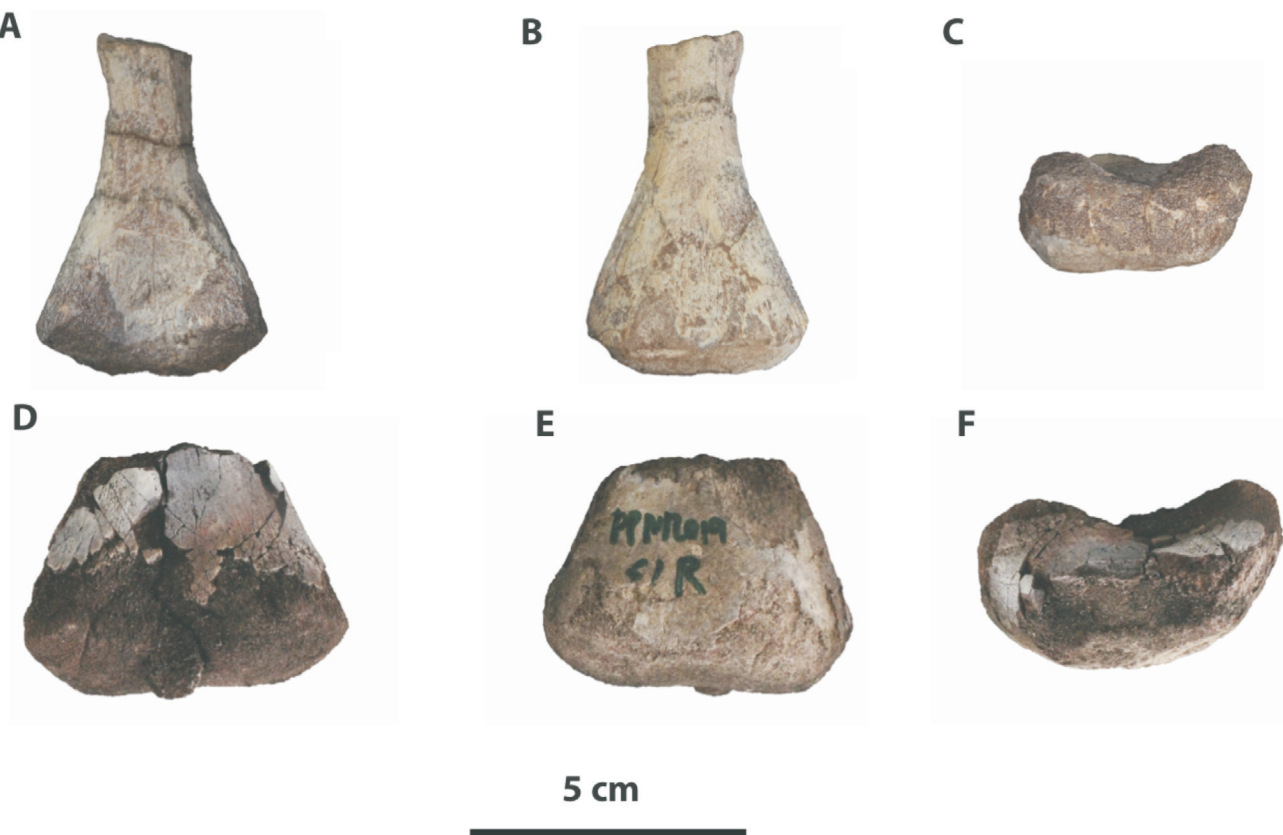


Figure 5. Comparison of PPM2019-51R/C and *Lystrosaurus* left femur FMNH UR 2708. *Lystrosaurus* left femur FMNH UR 2708: A, posterior view; B, anterior view; C, distal view. Dicynodontia indet. left femur (PPM2019-51R/C) from the Fubué Formation of the Metangula Graben (Mozambique): D, posterior view; E, anterior view; F, distal view.

sion (char 28:0); there is a distinct lateral caniniform buttress (char 29:1); there is no keel-like extension of the palatal rim posterior to the caniniform process (char 30:0); and there is no postcaniniform crest (char 31:0). This character combination also is present in *Lystrosaurus* spp. and *Euptychognathus*. However, the consensus tree did not recover a monophyletic Lystrosauridae. Instead, PPM2019-51R/A, *Lystrosaurus* spp. and *Euptychognathus* formed a polytomy near the base of Dicynodontida. Relative Bremer group supports within Bidentalalia are generally low for the strict consensus tree (<50), and for the clade including PPM2019-51R/A 36. Similarly, GC values (i.e. a measure that indicates differences in frequency between a group and the most frequent contradictory group, varying between -100 or maximum contradiction and 100 or maximum support) are low for the clade including PPM2019-51R/A (5). We attribute the low values to the fact that very few characters could be coded. Nevertheless, four of our seven most parsimonious trees still recovered PPM2019-51R/A within a monophyletic *Lystrosaurus* (Supplementary Data 3).

DISCUSSION

As is the case for many of the 'Karoo' basins of southern and eastern Africa, tetrapod fossils have been known from the Metangula Graben for several decades (Borges *et al.* 1953; also see review in Araújo *et al.* 2018a), but the vertebrate palaeontology of the basin has received much less recent attention than the nearby Luangwa Basin of Zambia and the Ruhuhu Basin of Tanzania. By far the

most commonly reported tetrapod from the Metangula Graben is the dicynodont *Endothiodon* (Antunes 1975; Latimer *et al.* 1995; Macungo *et al.* 2020), but this taxon has a relatively long range in the South African Karoo Basin (e.g. Smith *et al.* 2012; Day & Smith 2020), giving it limited biostratigraphic utility. Castanhinha *et al.* (2013) suggested that the K5 Formation could be correlated with the *Cistecephalus* Assemblage Zone of the South African Karoo Basin based on the co-occurrence of a humerus that they attributed to the dicynodont *Oudenodon* with specimens of *Endothiodon*, but the humerus had relatively few diagnostic features. In this context the results we report here significantly improve our understanding of the ages of the Metangula Graben tetrapods.

In the South African Karoo Basin, radiometrically-dated ash beds dated to 256.6 and 255.2 Mya bracket the strata assigned to the *Cistecephalus* Assemblage Zone (Rubidge *et al.* 2013; Smith 2020), and a third radiometric date constrains the underlying *Tropidostoma-Gorgonops* Subzone of the *Endothiodon* Assemblage Zone (AZ) to be less than 259.26 Mya (Day *et al.* 2015; Day & Smith 2020). Our maximum depositional age of 258.85 Mya for the K5c Member implies that a correlation between this member and the *Tropidostoma-Gorgonops* Subzone is likely more accurate. Although the most common components of the *Tropidostoma-Gorgonops* Subzone fauna (*Diictodon*, *Pristerodon*, *Emydops*, *Tropidostoma*; Smith *et al.* 2012, Day & Smith 2020) have not yet been discovered in Mozambique, the high abundance of *Endothiodon* in the K5 Formation is consistent with its higher relative abundance in the

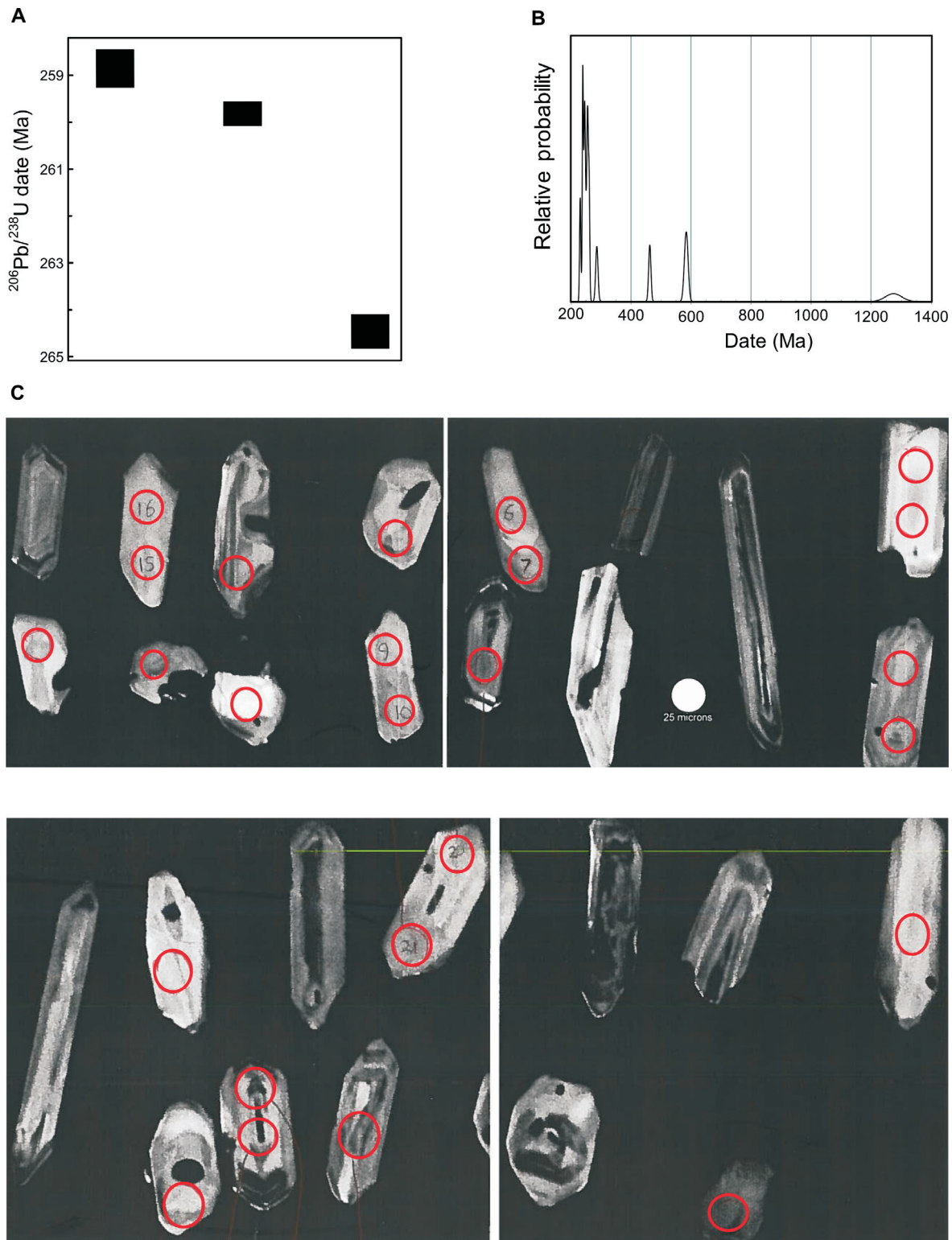


Figure 6. A, Plot of $^{206}\text{Pb}/^{238}\text{U}$ dates from grains of analysed by CA-TIMS. Plotted with Isoplot 3.0 (Ludwig 2003). Error bars are at 2σ . B, Probability density plot of LA-ICPMS U-Pb dates from zircon from sample PPM2012-12. Plotted with Isoplot 3.0 (Ludwig 2003). C, Cathodoluminescence images of zircon. Red circles indicate where the zircons have been sampled. For the complete analytical dataset see Supplementary Data 1 (LA-ICPMS) and Supplementary Data 2 (CA-TIMS).

Endothiodon AZ than in the *Cistecephalus* AZ (Day & Smith 2020; Smith 2020). The purported *Oudenodon* humerus from the basin (BP1/5749) might represent an early occurrence of the genus (*Oudenodon* is known from the upper *Tropidostoma-Gorgonops* Subzone in the South African Karoo; Botha & Angielczyk 2007; Day & Smith 2020) or a record of another cryptodont dicynodont such as *Tropidostoma* itself or *Bulbasaurus*, which would be expected to

have generally similar postcranial anatomy. Given the new age information, we now consider an identification of Cryptodontia indet. to be a preferable identification for BP1/5749.

The Permian-Triassic boundary in the Metangula Graben has been placed at the contact of the K6 Formation and the overlying Mount Lilonga (Ksa) Formation, which is accompanied by a significant facies change (Verniers

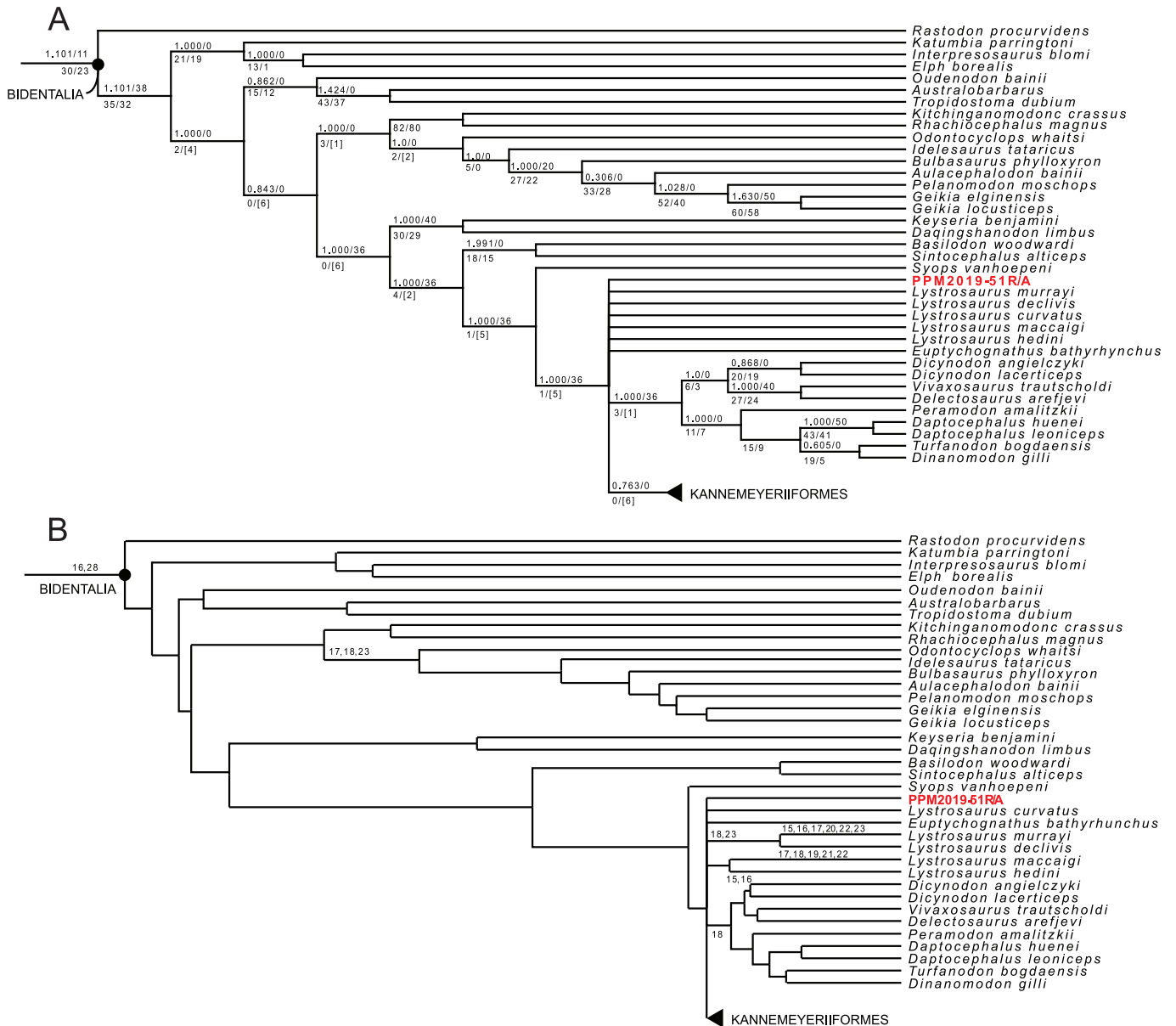


Figure 7. Strict consensus trees of the seven most parsimonious trees resulting from the phylogenetic analysis. The trees have been trimmed to facilitate visualization, for the complete trees see Supplementary Data 3, character matrix can be found in Supplementary Data 4. The two topologies of the PPM2019-51R/A specimen resulting from this analysis can be visualized in Supplementary Data 3 (bottom trees), where the specimen can be recovered within a monophyletic *Lystrosaurus* clade or as a sister taxon with *Eptychognathus*. **A**, Strict consensus tree with Bremer supports (from 62514 trees, cut 0.000)/Relative Bremer supports (from 42260 trees, cut 0), above branches; and group frequencies, after 100 replicates, cut = 50 (tree 0) for symmetric resampling ($P=33$)/GC values, after 100 replicates, cut = 0, below branches. **B**, Maxillary synapomorphies based on Kammerer (2019) character list.

et al. 1989). Unfortunately, our detrital zircon samples from the uppermost K6 Formation and the Mount Lilonga Formation only produced recycled zircons of much greater antiquity that could not meaningfully constrain the ages of these units. However, the discovery of *Lystrosaurus*-like dicynodonts in the Fubué Formation, which overlies the Mount Lilonga Formation, provides new information on the potential placement of the Permian-Triassic Boundary in the Metangula Graben. Additional refinement of the ages and biostratigraphic correlations of the K6, Mount Lilonga, and Fubué formations will be facilitated by new specimens discovered during the 2019 PaleoMoz expedition in the K6 Formation that are currently under study. Apart from the highly unusual Permian-Triassic Malagasy fauna (e.g. Ketchum & Barrett

2004), the discovery of *Lystrosaurus*-like fossils in the Metangula Graben make it the first 'Karoo' basin outside of South Africa to preserve a likely Early Triassic tetrapod assemblage, raising the possibility that it can provide new insight into the timing, causes, and effects of the end-Permian extinction in the terrestrial realm.

ABBREVIATIONS

Institutional

PPM PaleoMoz Project

NMQR National Museum Bloemfontein, Bloemfontein, South Africa.

SAM Iziko Museums of South Africa, Cape Town, South Africa.

PIN Paleontological Institute, Moscow, Russia

IVPP Institute for Vertebrate Paleontology, and Paleoanthropology, Beijing, China

Anatomical

ant r anterior ramus of the maxilla

can b	caniniform buttress
can p	caniniform process
lab f	labial fossa
lc	lateral condyle
mc	medial condyle
premax r	premaxillary recess
zyg n	zygomatic notch

General

LA-ICPMS	laser ablation inductively coupled plasma mass spectrometry
CL	cathodoluminescence
CA-TIMS	chemical abrasion isotope dilution thermal ionization mass spectrometry

Financial support was provided by the Museu Nacional de Geologia and by the Fundação para a Ciência e a Tecnologia (R.A. postdoctoral fellowship SFRH/BPD/96205/2013), FCT - AGA KHAN Development Network grant number 333206718, National Geographic Society grant number CP-109R-17. We would also like to thank Debra Pierce for selecting the zircon grains for dating, Luís Macuango for hosting us in Niassa, and Patrícia Pinheiro and Filipa Ferrão for financial management of the PaleoMoz Project. Christian Kammerer and Bruce Rubidge provided helpful reviews of the manuscript.

ORCID iDs

R. Araújo:	 orcid.org/0000-0001-5058-2983
Z. Macungo:	 orcid.org/0000-0002-2368-5917
R.M.H. Smith:	 orcid.org/0000-0001-6806-1983

REFERENCES

- ABDALA, F. & SMITH, R.M.H. 2009. A Middle Triassic cynodont fauna from Namibia and its implications for the biogeography of Gondwana. *Journal of Vertebrate Paleontology* **29**(3), 837–851.
- ANGIELCZYK, K.D. & RUBIDGE, B.S. 2013. Skeletal morphology, phylogenetic relationships and stratigraphic range of *Eosimops newtoni* Broom, 1921, a ptylaecephalid dicynodont (Therapsida, Anomodontia) from the Middle Permian of South Africa. *Journal of Systematic Palaeontology* **11**(2), 191–231.
- ANGIELCZYK, K.D., HUERTAS, S., SMITH, R.M.H., TABOR, N.J., SIDOR, C.A., STEYER, J.-S., TSUJI, L.A. & GOSTLING, N.J. 2014a. New dicynodonts (Therapsida, Anomodontia) and updated tetrapod stratigraphy of the Permian Ruhuhu Formation (Songea Group, Ruhuhu Basin) of southern Tanzania. *Journal of Vertebrate Paleontology* **34**, 1408–1426.
- ANGIELCZYK, K.D., STEYER, J.-S., SIDOR, C.A., SMITH, R.M.H., WHATLEY, R.L. & TOLAN, S. 2014b. Permian and Triassic dicynodont (Therapsida: Anomodontia) faunas of the Luangwa Basin, Zambia: taxonomic update and implications for dicynodont biogeography and biostratigraphy. In: Kammerer, C.F., Angielczyk, K.D. & Fröbisch, J. (eds), *Early Evolutionary History of the Synapsida*, 93–138. Dordrecht, Springer.
- ANTUNES, M.T. 1975. Sur quelques reptiles du Karroo de Maniamba, Mozambique. *Colloque International du Centre National de la Recherche Scientifique: Problèmes actuels de paléontologie-évolution des vertébrés* **218**, 371–378.
- ARAÚJO, R., CASTANHINHA, R. & COSTA JÚNIOR, L. 2012. A new anomodont taxon from the Mozambican Karoo (Niassa Province), Late Permian. In: Lopes, F.C., Andrade, A.I., Henriques, M.H., Quinta-Ferreira, M., Barata, M.T. & Pena dos Reis, R. (Coords). *Para Conhecer a Terra*, 142–150. Memórias e Notícias de Geociências no Espaço Lusófono. Imprensa da Universidade de Coimbra, Cap. 14.
- ARAÚJO, R., FERNANDEZ, V., RABBITT, R.D., EKDALE, E.G., ANTUNES, M.T., FRÖBISCH, J., MARTINS, R.M.S. 2018a. *Endothiodon cf. bathystoma* (Synapsida: Dicynodontia) bony labyrinth anatomy, variation and body mass estimates. *PLOS ONE* **13**(3), e0189883.
- ARAÚJO, R., NHAMUTOLE, N., MACUNGO, Z., MILISSE, D., BAMFORD, M. 2018b. Fossil tree hollows from a late Permian forest of the Matinde Formation (Tete, Mozambique). *Palaeontologia africana* **53**, 46–50.
- BENOIT, J., ANGIELCZYK, K.D., MIYAME, J.A., MANGER, P., FERNANDEZ, V. & RUBIDGE, B. 2018. Evolution of facial innervation in anomodont therapsids (Synapsida): insights from X-ray computerized microtomography. *Journal of Morphology* **279**, 673–701.
- BORGES, A., NUNES, A.F. & FREITAS, F. 1954 Contribution to the data on the Karroo of Portuguese Lake Nyasa. *Congr. Géol. Intern., Comptes rendus 19c session, Alger, 1952. Associations des Services Géologiques de l'Afrique* **21**, 83–91.
- BOTHA, J. & ANGIELCZYK, K.D. 2007. An integrative approach to distinguishing the Late Permian dicynodont species *Oudenodon bainii* and *Tropidostoma microtrema* (Therapsida: Anomodontia). *Palaeontology* **50**(5), 1175–1209.
- BOTHA, J., HUTTENLOCKER, A.K., SMITH, R.M.H., PREVEC, R., VIGLIETTI, P. & MODESTO, S.P. 2020. New geochemical and palaeontological data from the Permian-Triassic boundary in the South African Karoo Basin test the synchronicity of terrestrial and marine extinctions. *Palaeogeography, Palaeoclimatology, Palaeoecology* **540**, 109467.
- BREMER, K.R. 1994. Branch support and tree stability. *Cladistics* **10**(3), 295–304.
- BROOM, R. 1903. On the classification of the theriodonts and their allies. *Report of the South African Association for the Advancement of Science* **1**, 286–294.
- BROOM, R. 1905. On the use of the term Anomodontia. *Albany Museum Records* **1**, 266–269.
- CASTANHINHA, R., ARAÚJO, R., JÚNIOR, L.C., ANGIELCZYK, K.D., MARTINS, G.G., MARTINS, R.M., CHAOUIYA, C., BECKMANN, F. & WILDE, F. 2013. Bringing dicynodonts back to life: paleobiology and anatomy of a new emydopoid genus from the Upper Permian of Mozambique. *PLOS ONE* **8**(12), e80974.
- CONDON, D.J., SCHOENE, B., McLEAN, N.M., BOWRING, S.A., PARRISH, R. 2015. Metrology and traceability of U-Pb isotope dilution geochronology (EARTHTIME Tracer Calibration Part I): *Geochimica et Cosmochimica Acta* **164**, 464–480.
- CROWLEY, J.L., SCHOENE, B., BOWRING, S.A. 2007. U-Pb dating of the Bishop Tuff at the millennial scale: *Geology* **35**, 1123–1126.
- DAY, M.O. & SMITH, R.M.H. 2020. Biostratigraphy of the *Endothiodon* Assemblage Zone (Beaufort Group, Karoo Supergroup), South Africa. *South African Journal of Geology* **123**, 165–180.
- DAY, M.O., RAMEZANI, J., BOWRING, S.A., SADLER, P.M., ERWIN, D.H., ABDALA, F. & RUBIDGE, B.S. 2015. When and how did the terrestrial mid-Permian mass extinction occur? Evidence from the tetrapod record of the Karoo Basin, South Africa. *Proceedings of the Royal Society B: Biological Sciences* **282**, 20150834.
- DEFAUW, S.L. 1986. *The appendicular skeleton of African dicynodonts*. Unpublished Ph.D. thesis, Wayne State University, U.S.A.
- DESÓJO, J.B., FIORELLI, L.E., EZCURRA, M.D., MARTINELLI, A.G., RAMEZANI, J., DA ROSA, Á.A., von BACZKO, M.B., TROTTEYN, M.J., MONTEFELTRO, F.C., EZPELETA, M., LANGER, M.C. 2020. The Late Triassic Ischigualasto Formation at Cerro Las Lajas (La Rioja, Argentina): fossil tetrapods, high-resolution chronostratigraphy, and faunal correlations. *Scientific Reports* **10**(1), 1–34.
- ELTINK, E., DA-ROSA, Á.A.S. & DIAS-DA-SILVA, S. 2017. A capitosauroid from the Lower Triassic of South America (Sanga do Cabral Supersequence: Paraná Basin), its phylogenetic relationships and biostratigraphic implications. *Historical Biology* **29**, 863–874.
- EZCURRA, M.D., VELOZO, P., MENEGHEL, M. & PIÑEIRO, G. 2015. Early archosauromorph remains from the Permo-Triassic Buena Vista Formation of north-eastern Uruguay. *PeerJ* **3**, e776.
- FLORES, D., NHAMUTOLE, N., MILISSE, D., SUÁREZ-RUIZ, I. & ARAÚJO, R. 2019. A petrographic approach to a newly found lignite outcrop from Bilene (Gaza, Mozambique). *Journal of African Earth Sciences* **156**, 68–74.
- FRANCISCHINI, H., DENTZIEN-DIAS, P., LUCAS, S.G. & SCHULTZ, C.L. 2018. Tetrapod tracks in Permo-Triassic eolian beds of southern Brazil. *PeerJ* **6**, e4764.
- GASTALDO, R.A., KAMO, S.L., NEVELING, J., GEISSMAN, J.W., BAMFORD, M. & LOOY, C.V. 2015. Is the vertebrate-defined Permian-Triassic boundary in the Karoo Basin, South Africa, the terrestrial expression of the end-Permian marine event? *Geology* **43**, 939–942.
- GASTALDO, R.A., J. NEVELING, LOOY, C.V., BAMFORD, M.K., KAMO, S.L. & GEISSMAN, J.W. 2017. Paleontology of the Blaauwwater 67 and 65 farms, South Africa: testing the *Daptocephalus/Lystrosaurus* biozone boundary in a stratigraphic framework. *Palaios* **32**, 349–366.
- GASTALDO, R.A., NEVELING, J., GEISSMAN, J.W. & KAMO, S.L. 2018. A lithostratigraphic and magnetostratigraphic framework in a geochronologic context for a purported Permian-Triassic boundary section at Old (West) Lootsberg Pass, Karoo Basin, South Africa. *Geological Society of America Bulletin* **130**, 1411–1438.
- GASTALDO, R.A., NEVELING, J., GEISSMAN, J.W. & LI, J. 2019a. A multidisciplinary approach to review the vertical and lateral facies relationships of the purported vertebrate-defined terrestrial Permian-Triassic boundary interval at Bethulie, Karoo Basin, South Africa. *Earth-Science Reviews* **189**, 220–243.
- GASTALDO, R.A., NEVELING, J., GEISSMAN, J.W. & LOOY, C.V. 2019b. Testing the *Daptocephalus* and *Lystrosaurus* assemblage zones in a lithostratigraphic, magnetostratigraphic, and palynological framework in the Free State, South Africa. *Palaios* **34**, 542–561.
- GASTALDO, R.A., KUS, K., TABOR, N. & NEVELING, J. 2020. Calcic Vertisols in the upper *Daptocephalus* Assemblage Zone, Balfour Forma-

- tion, Karoo Basin, South Africa: implications for Late Permian Climate. *Journal of Sedimentary Research* **90**(6), 609–628.
- GERSTENBERGER, H. & HAASE, G. 1997. A highly effective emitter substance for mass spectrometric Pb isotope ratio determinations. *Chemical Geology* **136**, 309–312.
- GOLOBOFF, P.A. 1999. Analyzing large data sets in reasonable times: solutions for composite optima. *Cladistics* **15**(4), 415–428.
- GOLOBOFF, P.A. & FARRIS, J.S. 2001. Methods for quick consensus estimation. *Cladistics* **17**(1), S26–S34.
- GOLOBOFF, P.A., FARRIS, J.S., KÄLLERSJÖ, M., OXELMAN, B., RAMÍREZ, M.J. & SZUMIK, C.A. 2003. Improvements to resampling measures of group support. *Cladistics* **19**(4), 324–332.
- GOLOBOFF, P.A. & CATALANO, S.A. 2016. TNT version 1.5, including a full implementation of phylogenetic morphometrics. *Cladistics* **32**(3), 221–238.
- HEISS, J., CONDON, D.J., McLEAN, N. & NOBLE, S.R. 2012. ^{238}U - ^{235}U systematics in terrestrial uranium-bearing minerals. *Science* **335**, 1610–1614.
- JAFFEY, A.H., FLYNN, K.F., GLENDENIN, L.E., BENTLEY, W.C. & ESSLING, A.M. 1971. Precision measurements of half-lives and specific activities of ^{235}U and ^{238}U . *Physical Review C* **4**, 1889–1906.
- KETCHUM, H.F. & BARRETT, P.M. 2004. New reptile material from the Lower Triassic of Madagascar: implications for the Permian-Triassic extinction event. *Canadian Journal of Earth Sciences* **41**(1), 1–8.
- KAMMERER, C.F. 2019. Revision of the Tanzanian dicynodont *Dicynodon huenei* (Therapsida: Anomodontia) from the Permian Usili Formation. *PeerJ* **7**, e7420.
- KENNEDY, A.K., WOTZLAW, J.F., SCHALTEGGER, U., CROWLEY, J.L. & SCHMITZ, M. 2014. Eocene zircon reference material for microanalysis of U-Th-Pb isotopes and trace elements. *The Canadian Mineralogist* **52**(3), 409–421.
- KREUSER, T. 1995. Tectonic and climatic controls of lacustrine sedimentation in pre-rift and rift settings in the Permian-Triassic of East Africa. *Journal of Paleolimnology* **13**, 3–19.
- KING, G.M. 1981. The postcranial skeleton of *Robertia broomiana*, an early dicynodont (Reptilia, Therapsida) from the South African Karoo. *Annals of the South African Museum* **84**, 203–231.
- KROGH, T.E. 1973. A low contamination method for hydrothermal decomposition of and extraction of U and Pb for isotopic age determination. *Geochimica et Cosmochimica Acta* **37**, 485–494.
- LATIMER, E.M., GOW, C.E. & RUBIDGE, B.S. 1995. Dentition and feeding niche of *Endothiodon* (Synapsida, Anomodontia). *Palaeontologia africana* **32**, 75–82.
- LUCAS, S.G. 2017. Permian tetrapod extinction events. *Earth-Science Reviews* **170**, 31–60.
- LUDWIG, K.R. 2003. *User's Manual for Isoplot 3.00*. Berkeley, CA, Berkeley Geochronology Center, 70 pp.
- MACUNGO Z., LOIDEI I., ZUNGUZA S., NHAMUTOLE N., MAHARAJ I.E.M., MUGABE J., ANGIELCZYK K.D. & ARAÚJO R. 2019. *Endothiodon* (Therapsida, Anomodontia) specimens from the middle/late Permian of the Metangula Graben (Niassa Province, Mozambique) increase complexity to the taxonomy of the genus. *Journal of African Earth Sciences* **163**, 103647.
- MATTINSON, J.M. 2005. U-Pb chemical abrasion ("CA-TIMS") method: combined annealing and multi-step partial dissolution analysis for improved precision and accuracy of ages. *Chemical Geology* **220**, 47–66.
- MODESTÓ, S.P. & BOTHA-BRINK, J. 2010. Problems of correlation of South African and South American tetrapod faunas across the Permian-Triassic boundary. *Journal of African Earth Sciences* **57**, 242–248.
- OSBORN, H.F. 1903. On the primary division of the Reptilia into two sub-classes, Synapsida and Diapsida. *Science* **17**, 275–276.
- OWEN, R. 1860. On the orders of fossil and recent Reptilia and their distribution in time. *Report of the British Association for the Advancement of Science* **1859**, 153–166.
- PEECOOK, B.R., SMITH, R.M. & SIDOR, C.A. 2019. A novel archosauromorph from Antarctica and an updated review of a high-latitude vertebrate assemblage in the wake of the end-Permian mass extinction. *Journal of Vertebrate Paleontology* **38**(6), e1536664.
- PINEIRO, G., FERIGOLO, J., RIBEIRO, A.M., VELOZO, P. 2015. Reassessing the affinities of vertebral remains from Permo-Triassic beds of Gondwana. *Comptes Rendus Palevol* **14**, 387–401.
- RUBIDGE, B.S., ERWIN, D.H., RAMEZANI, J., BOWRING, S.A., DE KLERK, W.J. 2013. High-precision temporal calibration of Late Permian vertebrate biostratigraphy: U-Pb zircon constraints from the Karoo Supergroup, South Africa. *Geology* **41**, 363–366.
- RAY, S. 2005. *Lystrosaurus* (Therapsida, Dicynodontia) from India: taxonomy, relative growth and cranial dimorphism. *Journal of Systematic Palaeontology* **3**, 203–221.
- RAY, S. 2006. Functional and evolutionary aspects of the postcranial anatomy of dicynodonts (Synapsida, Therapsida). *Palaeontology* **49**, 1263–1286.
- RAY, S., CHINSAMY, A. 2003. Functional aspects of the postcranial anatomy of the Permian dicynodont *Diictodon* and their ecological implications. *Palaeontology* **46**, 151–183.
- ROZEFELDS, A.C., WARREN, A., WHITFIELD, A. & BULL, S. 2011. New evidence of large Permo-Triassic dicynodonts (Synapsida) from Australia. *Journal of Vertebrate Paleontology* **31**, 1158–1162.
- SCHMITZ, M.D. & SCHOENE, B. 2007. Derivation of isotope ratios, errors and error correlations for U-Pb geochronology using ^{205}Pb - ^{235}U - ^{233}U -spiked isotope dilution thermal ionization mass spectrometric data. *Geochemistry, Geophysics, Geosystems* **8**, Q08006.
- SLÁMA, J., KOŠLER, J., CONDON, D.J., CROWLEY, J.L., GERDES, A., HANCHAR, J.M., HORSTWOOD, M.S.A., MORRIS, G.A., NASDALA, L., NORBERG, N., SCHALTEGGER, U., SCHOENE, B., TUBRETT, M.N. & WHITEHOUSE, M.J. 2008. Plešovice zircon — A new natural reference material for U-Pb and Hf isotopic microanalysis. *Chemical Geology* **249**, 1–35.
- SIDOR, C.A., ANGIELCZYK, K.D., WEIDE, D.M., SMITH, R.M.H., NESBITT, S.J. & TSUJI, L.A. 2010. Tetrapod fauna of the lowermost Usili Formation (Songea Group, Ruhuhu Basin) of southern Tanzania, with a new burnetiid record. *Journal of Vertebrate Paleontology* **30**, 696–703.
- SMITH, R.M.H. 1990. Alluvial palaeosols and pedofacies sequences in the Permian Lower Beaufort of the southwestern Karoo Basin, South Africa. *Journal of Sedimentary Petrology* **60**, 258–276.
- SMITH, R.M.H. 2000. Sedimentology and taphonomy of Late Permian vertebrate fossil localities in southwestern Madagascar. *Palaeontologia africana* **36**, 25–41.
- SMITH, R.M.H. 2020. Biostratigraphy of the *Cistecephalus* Assemblage Zone (Beaufort Group, Karoo Supergroup), South Africa. *South African Journal of Geology* **123**, 181–190.
- SMITH, R.M.H., RUBIDGE, B.S. & VAN DER WALT, M. 2012. Therapsid biodiversity patterns and paleoenvironments of the Karoo Basin, South Africa. In: Chinsamy-Turan, A. (ed.), *Forerunners of Mammals*, 31–62. Bloomington and Indianapolis, Indiana University Press.
- SMITH, R.M.H. & BOTHA-BRINK, J. 2014. Anatomy of a mass extinction: sedimentological and taphonomic evidence for drought-induced die-offs at the Permo-Triassic boundary in the main Karoo Basin, South Africa. *Palaeogeography, Palaeoclimatology, Palaeoecology* **396**, 99–118.
- SMITH, R.M.H., SIDOR, C.A., ANGIELCZYK, K.D., NESBITT, S.J. & TABOR, N.J. 2018. Taphonomy and paleoenvironments of Middle Triassic bone accumulations in the Lifua Member of the Manda Beds, Songea Group (Ruhuhu Basin), Tanzania. In: Sidor, C.A. & Nesbit, S.J. (eds). *Vertebrate and Climatic Evolution in the Triassic Rift Basins of Tanzania and Zambia*, 65–79. Society of Vertebrate Paleontology Memoir 17. *Journal of Vertebrate Paleontology* **37**(6, Supplement).
- VALDIYA, K.S. 2016. *The Making of India: Geodynamic Evolution* (2nd edn). Springer, Cham.
- VERNERS, J., JOURDAN, P.P., PAULIS, R.V., FRASCA-SPADA, L. & DE BOCK, F.R. 1989. The Karroo Graben of Metangula, northern Mozambique. *Journal of African Earth Sciences (and the Middle East)* **9**(1), 137–158.
- VIGLIETTI, P.A., SMITH, R.M.H. & RUBIDGE, B.S. 2018a. Changing palaeoenvironments and tetrapod populations in the *Daptocephalus* Assemblage Zone (Karoo Basin, South Africa) indicate early onset of the Permo-Triassic mass extinction. *Journal of African Earth Sciences* **138**, 102–111.
- WARREN, A.A., RUBIDGE, B.S., STANISTREET, I.G., STOLLHOFEN, H., WANKE, A., LATIMER, E.M., MARSICANO, C. A. & DAMIANI, R. J. 2001. Oldest known stereospondylous amphibian from the Early Permian of Namibia. *Journal of Vertebrate Paleontology* **21**(1), 34–39.
- WARREN, A.A., DAMIANI, R.J. & YATES, A.M. 2006. The South African stereospondyl *Lydekkerina huxleyi* (Tetrapoda, Temnospondyli) from the Lower Triassic of Australia. *Geological Magazine* **143**, 877–886.
- WARREN, A.A., ROZEFELDS, A.C. & BULL, S. 2011. Tupilakosaur-like vertebrae in *Bothriechis australis*, an Australian brachyopid stereospondyl. *Journal of Vertebrate Paleontology* **31**, 738–753.
- WATSON, E.B., WARK, D.A. & THOMAS, J.B. 2006. Crystallization thermometers for zircon and rutile. *Contributions to Mineralogy and Petrology* **151**, 413–433.
- WEISSMANN, G.S., HARTLEY, A.J., NICHOLS, G.J., SCUDERI, L.A., OLSON, M., BUEHLER, H. & BANTEAH, R. 2010. Fluvial form in modern continental sedimentary basins: distributive fluvial systems. *Geology* **38**, 39–42.
- WHITNEY, M.R., TSE, Y.T. & SIDOR, C.A. 2019. Histological evidence of trauma in tusks of southern African dicynodonts. *Palaeontologia africana* **53**, 75–80.
- YEMANE, K. & KELTS, K. 1990. A short review of paleoenvironments for Lower Beaufort (Upper Permian) Karoo sequences from southern to central Africa – a major Gondwana lacustrine period. *Journal of African Earth Sciences* **10**, 169–186.